

See discussions, stats, and author profiles for this publication at: <https://www.researchgate.net/publication/222673607>

# A six-axis single-stage active vibration isolator based on Stewart platform

Article in *Journal of Sound and Vibration* · March 2007

DOI: 10.1016/j.jsv.2006.07.050

---

CITATIONS

67

---

READS

125

8 authors, including:



[A. Preumont](#)

Université Libre de Bruxelles

246 PUBLICATIONS 3,323 CITATIONS

[SEE PROFILE](#)



[Mihaïta Horodincă](#)

Gheorghe Asachi Technical University of Iasi

49 PUBLICATIONS 312 CITATIONS

[SEE PROFILE](#)



[Frédéric Bossens](#)

Standard Chartered

19 PUBLICATIONS 393 CITATIONS

[SEE PROFILE](#)



[Ahmed Mohammed Abu Hanieh](#)

Birzeit University

30 PUBLICATIONS 229 CITATIONS

[SEE PROFILE](#)

All content following this page was uploaded by [A. Preumont](#) on 24 December 2013.

The user has requested enhancement of the downloaded file. All in-text references [underlined in blue](#) are added to the original document and are linked to publications on ResearchGate, letting you access and read them immediately.

# A SIX-AXIS SINGLE STAGE ACTIVE VIBRATION ISOLATOR BASED ON STEWART PLATFORM

A. Preumont, M. Horodincea, I. Romanescu, B. de Marneffe, M. Avraam, A. Deraemeker,\*  
F. Bossens † A. Abu Hanieh ‡

\* ULB, Active Structures Laboratory, 1000 Brussels, Belgium  
e-mail: Andre.Preumont@ulb.ac.be

† Micromega Dynamics, S.A., 4000 Liège, Belgium

‡ Birzeit University, Palestine

**Keywords:** Vibration isolator, Gough-Stewart platform, Sky-hook damper, force feedback, decentralized control, parabolic flight.

**Abstract.** *This paper reports on a six-axis vibration isolator for space applications. It is divided into three parts. The first part recalls the principles of active isolation and summarizes the main theoretical results for multiple-axis decentralized control based on force feedback. The second part discusses the technology and describes the evolution of the design over the five years of this project. The third part is devoted to the identification of the transmissibility matrix and the performance evaluation; zero-gravity tests in parabolic flight are reported: the isolator is proved efficient in a frequency band between 5 Hz and 400 Hz, with a maximum attenuation of -40 dB between 50 Hz and 200 Hz.*

## 1 INTRODUCTION

Many applications in precision engineering would be impossible without a careful isolation of the process from the vibration environment. Examples are wafer stepper lithography machines, atomic force microscopes, space telescopes and interferometers, laser communication systems, etc.... This paper is concerned with the development of a vibration isolation interface for space applications [1,2], which attenuates the vibration transmission above some corner frequency, to protect the payload from the jitter induced by the various disturbance sources, such as the reaction wheel assembly, solar array drives, cryocoolers, etc..., while allowing the low-frequency attitude control torque to be transmitted.

Passive isolation [3] is appropriate for many applications, it generally consists of one or several stages of mass-spring-damper systems introduced in the propagation path, whose parameters are adjusted to achieve the desired corner frequency and a reasonable compromise between the amplification at resonance and the high-frequency attenuation. The passive damping is necessary to limit the amplification at resonance, but it tends to reduce the high-frequency attenuation of the isolation system. Active isolation has been introduced to resolve this conflict,

allowing to achieve simultaneously a low amplification at resonance and a large attenuation at high-frequency. The celebrated "sky-hook" damper [4,5] is a single-axis interface which, if inserted between two rigid bodies, allows to combine a -40 dB/decade attenuation rate at high frequency with a critical damping (no overshoot) at resonance. When inserted between rigid bodies, the sky-hook damper may be implemented with an acceleration (or velocity) feedback, or equivalently with force feedback. However, when inserted between two flexible structures, as is likely in space applications, it turns out that the force feedback implementation enjoys guaranteed stability properties that acceleration feedback lacks.

To fully isolate two rigid bodies with respect to each other, six single-axis isolator judiciously placed are needed; they can be controlled in a centralized or decentralized manner. For a number of space applications, generic multi-purpose isolators have been developed with a standard Gough-Stewart platform architecture [6-12], in which every leg of the platform consists of a single-axis isolator, connected to the base plates by spherical joints.

This paper considers only the decentralized feedback control approach which has attractive robustness properties and is shown to produce impressive performances, provided the mechanical design is properly done. More sophisticated control architecture may be considered [11], but at the price of reduced robustness. If the disturbance can be measured somewhere along its propagation path, a feedforward approach can be considered; this approach was followed in [6]. Finally, the isolation control loop discussed here can be imbedded in a global precision pointing control system; this topic is discussed in [12-15].

## 2 SKY-HOOK DAMPER

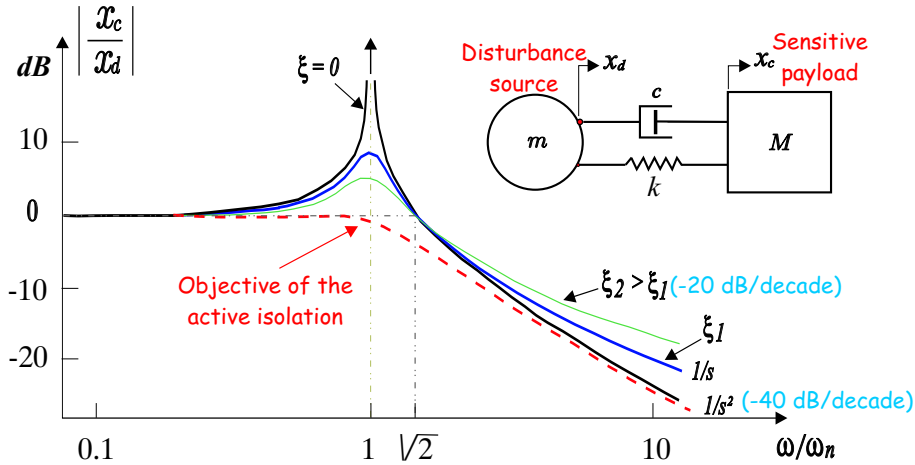


Figure 1. Transmissibility of the single-axis passive linear isolator, for various values of the damping

The transmissibility of a single-axis passive linear oscillator is given by

$$\frac{X_c(s)}{X_d(s)} = \frac{1 + 2\xi s/\omega_n}{1 + 2\xi s/\omega_n + (s/\omega_n)^2} \quad (1)$$

where  $s$  is the Laplace variable,  $\omega_n$  is the natural frequency and  $\xi$  the fraction of critical damping. The amplitude of the corresponding Frequency Response Function (FRF), obtained for  $s = j\omega_n$ , is represented in Fig.1 for various values of  $\xi$ . All the curves are larger than 1 for  $\omega < \sqrt{2}\omega_n$ , and smaller than 1 for  $\omega > \sqrt{2}\omega_n$ . Thus, the isolator attenuates the disturbance beyond the critical frequency  $\sqrt{2}\omega_n$ . For  $\xi = 0$ , the high frequency behavior of (1) is  $\sim 1/s^2$ , which means an asymptotic decay rate of -40 dB/decade, while very large amplitude occur near the corner frequency  $\omega_n$ . The damping reduces the amplitude at all frequencies below  $\sqrt{2}\omega_n$ , and in particular at the resonance  $\omega_n$ , but it increases the amplitude at all frequencies above  $\sqrt{2}\omega_n$ , reducing the asymptotic behavior to  $\sim 1/s$ , that is an asymptotic decay rate of -20 dB/decade.

The *sky-hook* damper is a feedback control strategy which allows to reduce the amplitude of the transmissibility at low frequency (below and near the corner frequency) without deteriorating its high-frequency behavior, and keeping an asymptotic decay rate of -40 dB/decade. The strategy is illustrated in Fig.2: The isolator consists of a spring (no damper) and a force actuator  $F_a$  acting in parallel; a sensor placed on the payload (accelerometer or geophone) allows to measure its absolute velocity  $sX_c(s)$ . The feedback control strategy consists of generating a control force proportional to the absolute velocity of the payload,  $F_a = -gsX_c(s)$ . From the payload point of view, this is equivalent to connecting it to a fixed point in space [called *sky* in Fig.2(b)] with a viscous damper of constant  $g$ .

Since the force applied to a rigid body is proportional to its acceleration, the acceleration feedback (or velocity feedback) may be replaced by a feedback based on a force sensor measuring the total interface force,  $F = Ms^2X_c(s)$  [Fig.2(c)]. The two control configurations are totally equivalent; they have the same open-loop transfer function (except for a constant factor); the root locus of the closed-loop system is shown in Fig.3; the closed-loop poles move on a circle. The transmissibility of the force feedback isolator reads:

$$\frac{X_c(s)}{X_d(s)} = \left[ \frac{M}{k}s^2 + \frac{M}{k}gs + 1 \right]^{-1} \quad (2)$$

which exhibits an attenuation rate of -40 dB/decade at high frequency. The feedback gain can be adjusted to achieve critical damping, meaning no amplification at the corner frequency.

If the two structures connected by the single-axis isolator are flexible, the force feedback and acceleration feedback implementations are no longer equivalent, and the corresponding open-loop transfer functions exhibit different pole/zero patterns. It has been shown that *if two arbitrary flexible, undamped structures are connected with a single-axis soft isolator with force feedback (Fig.4), the poles and zeros in the open-loop transfer function ( $F/F_a$ ) alternate on the imaginary axis [17,18]*. This property is maintained for lightly damped structures, except that the poles and zeros are slightly in the left-half plane instead of being on the imaginary axis. This guarantees that the feedback law  $F_a = -(g/s)F$  will be stable. Such a result does not exist for the acceleration feedback, and one can easily show on an example that this property is lost when the corner frequency of the suspension interferes with the flexible modes. Based on this result, we have opted for a force feedback implementation.

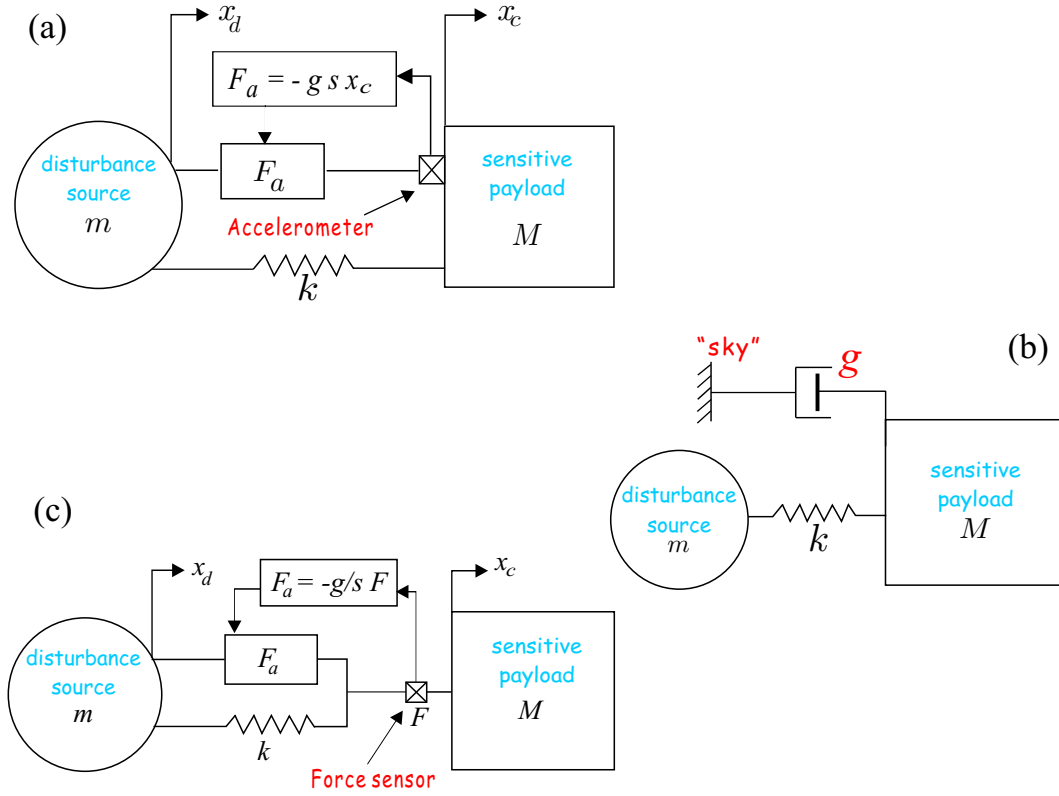


Figure 2. (a) Single-axis soft isolator with velocity feedback. (b) Equivalent sky-hook damper. (c) Force feedback isolator.

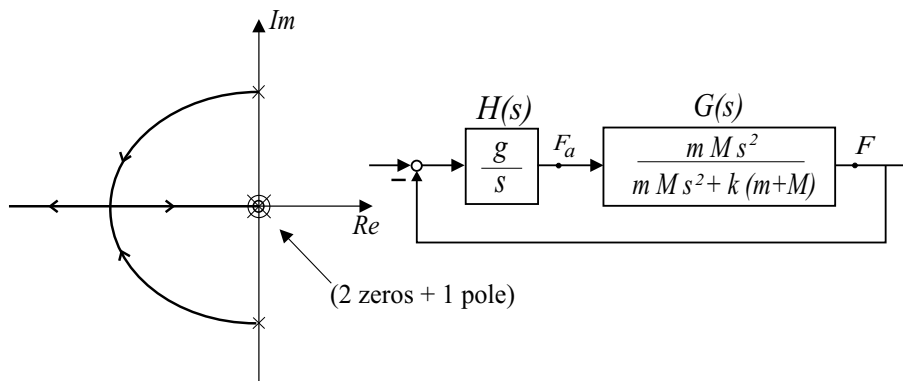


Figure 3. Root locus of the force feedback isolator connecting two rigid bodies.

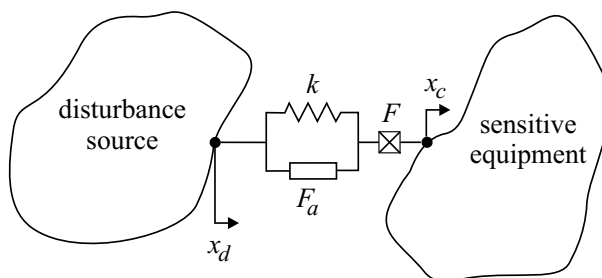


Figure 4. Two arbitrary flexible structures connected by a single-axis soft isolator with force feedback.

### 3 SIX-AXIS ISOLATOR

The single-axis isolator considered in the foregoing section combines an attenuation rate of -40 dB/decade with a tunable overshoot at resonance; the system can be made critically damped (no overshoot) by proper selection of the feedback gain  $g$ . If a force feedback implementation is used, the sky-hook damper has guaranteed stability, even if the structures to be isolated are flexible, and if the flexible modes and the suspension modes overlap. To fully isolate two rigid bodies with respect to each other, six single-axis isolators must be located judiciously. For simplicity reasons, we take the view that the same isolator is used along every axis, and that they are controlled in a decentralized manner. Two new problems arise: (i) The system does not have one, but six suspension modes, with generally different frequencies, and it will not be possible to achieve critical damping simultaneously for all suspension modes. (ii) Every single-axis isolator should be mounted on spherical joints, to allow the motion orthogonal to its own axis. However, backlash free spherical joints are difficult to realize and, in precision engineering, they are replaced by elastic joints which have a small rotary stiffness. Even small, the residual rotary stiffness has a strong effect on the closed-loop performance of the suspension, because it determines the transmission zeros, which are the asymptotic solution of the eigenvalue problem as  $g \rightarrow \infty$ .

An attractive architecture for a generic multi-purpose 6-axis isolator is that of a Gough-Stewart platform [16] (Fig.5), and several projects have been developed for space applications [6-12]. The system consists of 6 identical active struts connected to the end plates by spherical joints. Most existing projects, including this one, have opted for a *cubic* architecture [6], where the active struts are arranged in a mutually orthogonal configuration connecting the corners of a cube (Fig.6). This topology provides a uniform control capability and a uniform stiffness in all directions, and it minimizes the cross coupling amongst actuators and sensors of different legs (being orthogonal to each other). Figure 6 depicts the geometry of the hexapod and the numbering of the nodes and the struts; the base frame  $\{x_b, y_b, z_b\}$  has its origin at node 0; the payload frame  $\{x_r, y_r, z_r\}$  has its origin at the geometrical center of the hexapod, noted 8, and  $\vec{z}_r$  is perpendicular to the payload plate; the orientation of  $\vec{x}_r$  and  $\vec{y}_r$  is shown in Fig.6. If one neglects the flexibility of the struts and the bending stiffness of the flexible joints connecting it to the base and payload plates, the equations of motion can be obtained from rigid body dynamics.

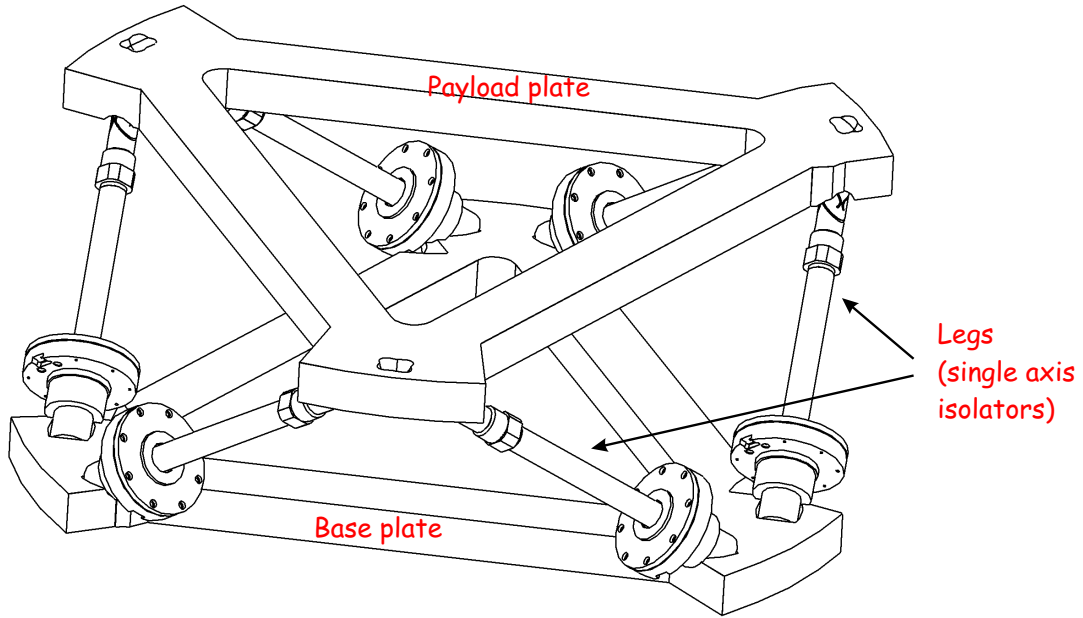


Figure 5. Multi-purpose soft isolator based on a Gough-Stewart platform.

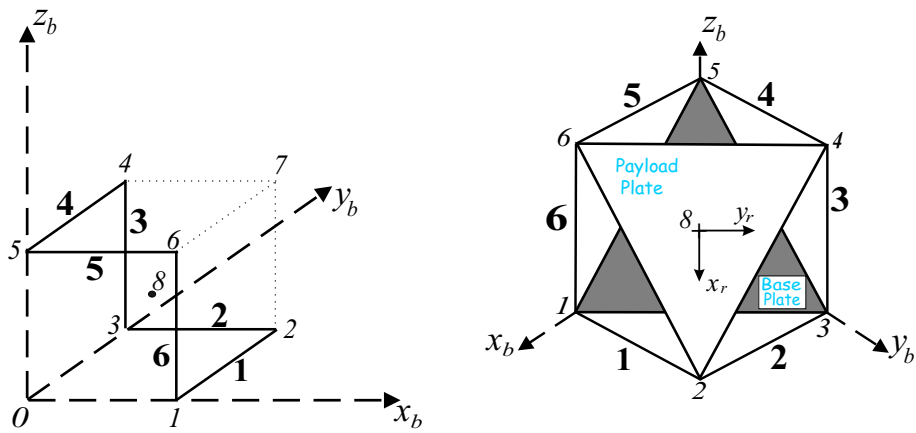


Figure 6. Geometry and coordinate systems for the cubic hexapod isolator. Number in bold indicate the struts.

Assume that the base plate is fixed and denote by  $B$  the projection matrix connecting the force acting along the strut axes and those in the payload plate axes  $\{x_r, y_r, z_r\}$ . One has

$$f = B(u - kq) \quad (3)$$

where  $f = (f_x, f_y, f_z, M_x, M_y, M_z)^T$  are the forces applied by the legs expressed in the payload axes,  $u = (u_1, \dots, u_6)^T$  the vector of active control forces in struts 1 to 6, and  $q = (q_1, \dots, q_6)^T$  the vector of leg extensions. In (3),  $k$  is the stiffness of the suspension spring, assumed the same for all legs.  $u - kq$  is the total force in the leg, sum of the control force  $u$  and the elastic restoring force in the spring. From the virtual work principle, the leg extensions and the small displacements and rotations of the payload plate,  $x = (x_r, y_r, z_r, \theta_x, \theta_y, \theta_z)^T$ , satisfy

$$q = B^T x \quad (4)$$

Substituting in (3) and writing the dynamic equilibrium on the payload, one finds

$$M\ddot{x} = Bu - kBB^T x$$

or

$$M\ddot{x} + kBB^T x = Bu \quad (5)$$

where  $M$  is the  $6 \times 6$  mass matrix of the payload

$$M = \begin{bmatrix} mI & 0 \\ 0 & J \end{bmatrix} \quad (6)$$

$m$  is the mass and  $J$  the inertia tensor of the payload in the payload frame. In (5),  $kBB^T$  is the stiffness matrix of the suspension, resulting exclusively from the axial stiffness of the suspension struts. In practice, however, the spherical joints are responsible of an additional contribution  $K_e$  (in this case, they can be viewed as flexible universal joints: low bending stiffness, high axial, shear and torsion stiffness, see below). The total stiffness matrix is  $kBB^T + K_e$  and Equ.(5) becomes

$$M\ddot{x} + (kBB^T + K_e)x = Bu \quad (7)$$

#### 4 DECENTRALIZED CONTROL

In order to benefit from the robustness properties discussed at the beginning of the paper, the control strategy consists of a decentralized sky-hook damper based on force feedback. The isolator is equipped with 6 force sensors measuring the total axial force in the various legs; the output equation is

$$y = u - kq = u - kB^T x \quad (8)$$

where  $y = (y_1, \dots, y_6)^T$  is the vector of the six force sensor outputs (the vector of control forces  $u$  and the leg extensions  $q$  have been defined earlier). Using a decentralized integral force feedback with the same gain  $g$  for every loop, the controller equation reads

$$u = H(s)y = -\frac{g}{s} y \quad (9)$$

( $g$  is a scalar in this case). Combining (8) and (9), one gets

$$u = \frac{g}{s+g} k B^T x \quad (10)$$

and, substituting in (7), the closed-loop characteristic equation reads

$$M\ddot{x} + (k B B^T + K_e)x = \frac{g}{s+g} k B B^T x \quad (11)$$

#### 4.1 Perfect joints

First, consider the case of perfect spherical joints,  $K_e = 0$ . In this case, Equ.(11) becomes

$$[M s^2 + \frac{s}{s+g} (k B B^T)] x = 0 \quad (12)$$

The free suspension modes are the solutions of (12) for  $g = 0$ . If one denotes  $\Phi$  the matrix of the suspension modes, normalized in such a way that  $\Phi^T M \Phi = I$ ,  $\Phi^T (k B B^T) \Phi = \Omega^2 = \text{diag}(\Omega_i^2)$ , (12) can be transformed into modal coordinates according to  $x = \Phi z$ . In modal coordinates, the characteristic equation (12) is reduced to a set of uncoupled equations

$$s^2 + \frac{s}{s+g} \Omega_i^2 = 0 \quad (13)$$

$$1 + g \frac{s}{s^2 + \Omega_i^2} = 0 \quad (14)$$

$i = 1, \dots, 6$ . The corresponding root locus is shown in Fig.7(a). It is identical to Fig.3 for a single axis isolator; however, unless the 6 natural frequencies of the suspension modes are identical, a given value of the gain  $g$  leads to different pole locations for the various modes, and it is not possible to achieve the same damping for all modes. Better, more balanced performances will be obtained if  $\Omega_1$  to  $\Omega_6$  are close to each other. It is recommended to locate the payload in such a way that the *modal spread*  $\Omega_6/\Omega_1$  is minimized [7].

#### 4.2 Real joints

Let us investigate the influence of the parasitic stiffness  $K_e$  introduced by the flexible joints. The closed-loop characteristic equation becomes in this case

$$[M s^2 + K_e + \frac{s}{s+g} (k B B^T)] x = 0 \quad (15)$$

The asymptotic solutions for high gain ( $g \rightarrow \infty$ ) are no longer at the origin  $s = 0$ , but satisfy the eigenvalue problem

$$(M s^2 + K_e)x = 0 \quad (16)$$

The solutions are the natural frequencies  $z_i$  of the system when the axial stiffness of the leg has been removed ( $k = 0$ ). This shift of the zeros from the origin to finite frequencies, Fig.7(b), has a substantial influence on the practical performances of the isolator, and justifies a careful design of the joints.

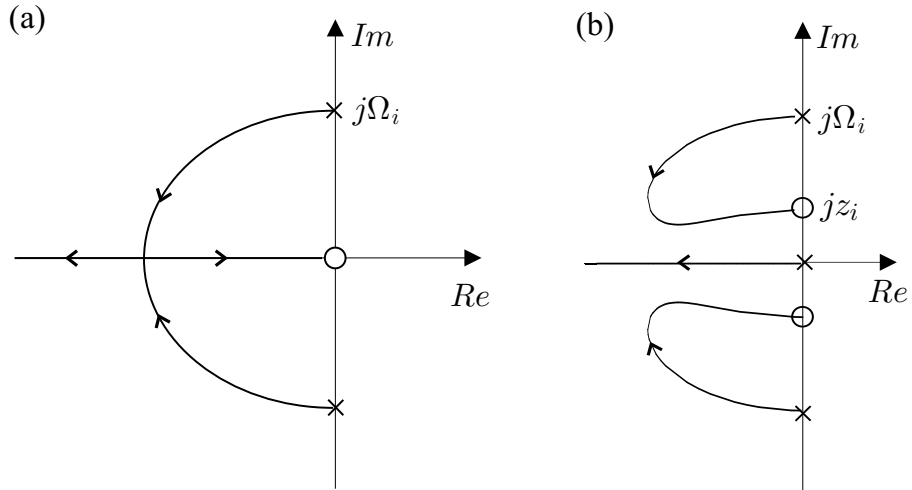


Figure 7. (a) Root locus of the suspension modes of the perfect six-axis isolator ( $K_e = 0$ ) with decentralized integral force feedback. (b) Effect of the stiffness of the flexible joints ( $K_e \neq 0$ ).

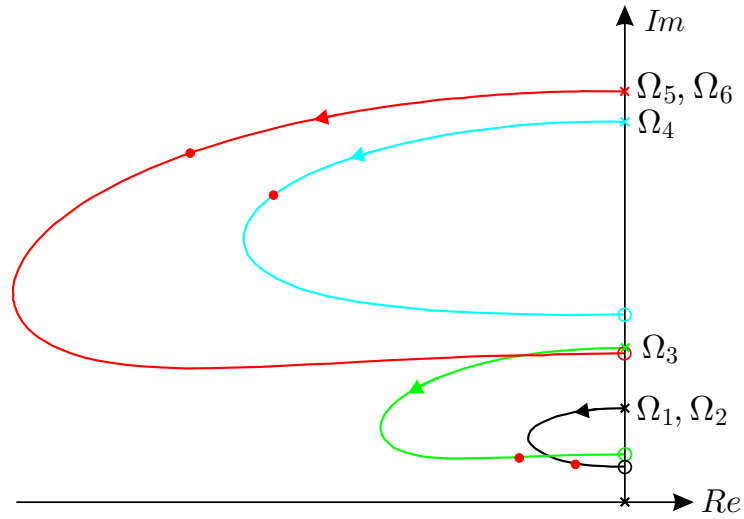


Figure 8. Typical root locus of a complete isolation system with real joints.

The combined effect of the modal spread and the joint stiffness is illustrated in Fig.8; there are only 4 different curves because of the symmetry of the system. The bullets correspond to the closed-loop poles for a fixed value of  $g$ ; they illustrate the fact that the various loops are travelled at different speeds as  $g$  increases. How this impacts the transmissibility is examined below.

Before closing this section, it is appropriate to mention two additional factors which reduce the closed-loop performances of the isolator:

(i) The integral controller (9) requires the addition of a high-pass filter (to avoid saturation), which impacts negatively the performances of the system. However, the detrimental effect of the high-pass filter can be minimized if its corner frequency is selected far enough below the lowest suspension mode.

(ii) The results of this section have been achieved assuming that the legs are massless and perfectly rigid, except in the axial direction. In practice, however, the legs have their own local dynamics which interfere with that of the isolator and impact significantly the transmissibility in the vicinity of the resonance frequency of the local modes and beyond. Maximizing the natural frequency of the local modes of the legs is a major challenge in the design of a six-axis isolator with broadband isolation capability. The leg design is discussed below.

## 5 LEG DESIGN

Figure 9 shows two conceptual designs which have been considered successively during this project. In the first design (Fig.9.a), the longitudinal motion and the axial stiffness are achieved with two parallel membranes mounted inside a cylinder which also supports the permanent magnet of the voice coil actuator. The stinger is attached to the center of the membranes; it supports the coil at one end, and the force sensor at the other end; two flexible joints are used to connect the leg, respectively to the base plate and to the payload plate. The various components were optimized to maximize the performance; this design was built and tested, including in parabolic flight in 2002 [19]; the isolator works in the frequency band 5-100 Hz with a maximum attenuation of about 20 dB near 50 Hz. However, this leg design was not able to pass the qualification tests (vibration during launch), because of the weakness of the flexible joints. This triggered the second design, with the objective of reducing the weight of the moving part of the leg assembly (Fig.9.b).

In the second design, the permanent magnet, which is the heaviest moving part in the previous design, has been removed from the leg and attached to the base plate. A single membrane acts simultaneously as spring and flexible joint on the base plate side. In this design, the coil axis is allowed to rotate with respect to the magnet axis, which necessitates an increase of the gap in the magnet. The stinger (made of carbon fibres) is attached to the center of the membrane; it supports the voice coil at one end, the force sensor at the other end, and is connected to the payload plate by a single flexible joint. This design reduces drastically (by a factor 8) the weight attached to the membrane and flexible tip. This configuration passed successfully the vibration tests. The natural frequency of the local mode is also raised drastically, leading to a dramatic improvement of the performances; the isolator works in the frequency band 5-400

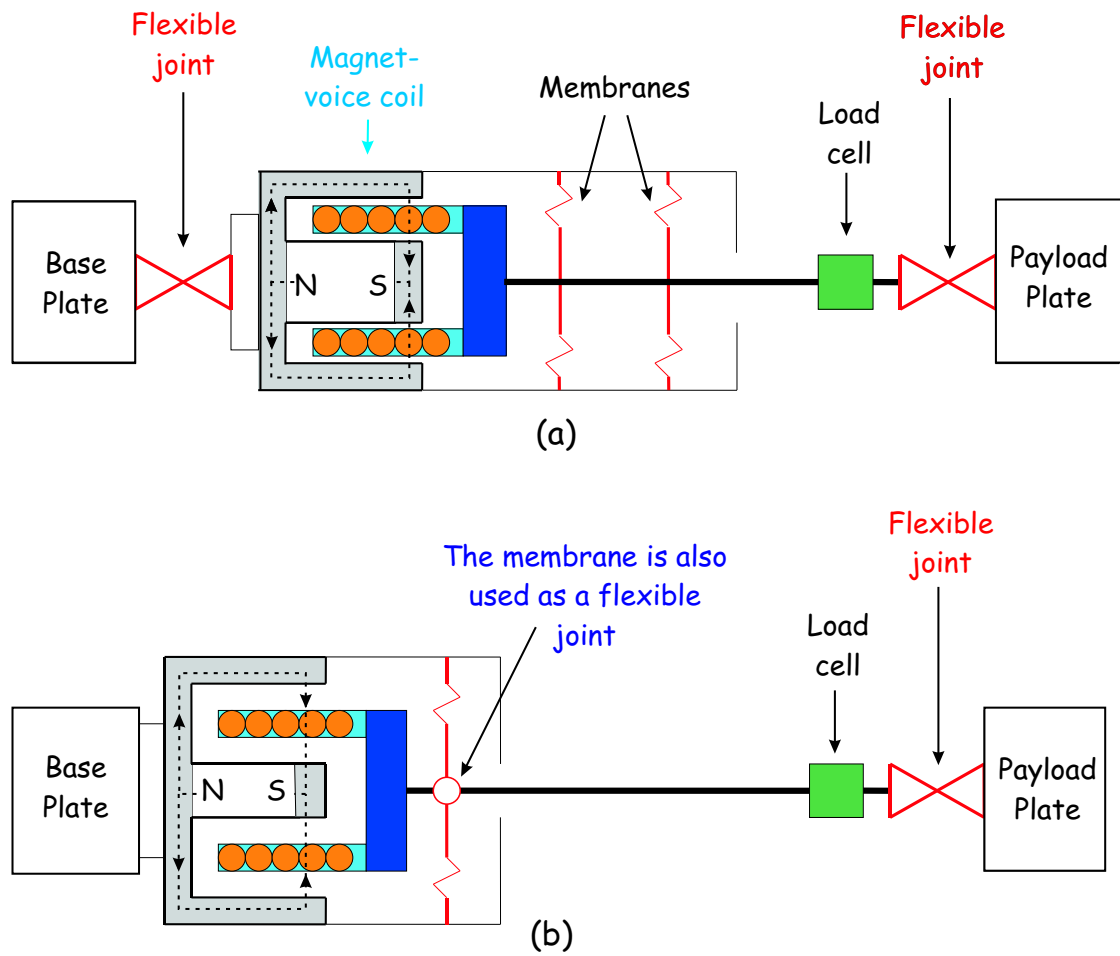


Figure 9. (a) Design # 1: 2 membranes, 2 flexible joints, magnet in the leg. (b) Design # 2: 1 membrane, 1 flexible joint, magnet in the base plate.

Hz with a maximum attenuation of about 40 dB near 100 Hz (see below). It is interesting to emphasize the fact that this considerable improvement has been achieved by mechanical design alone, without changing the control law (!). Figure 10 shows an exploded view of the leg of the second design; some details of the design follow:

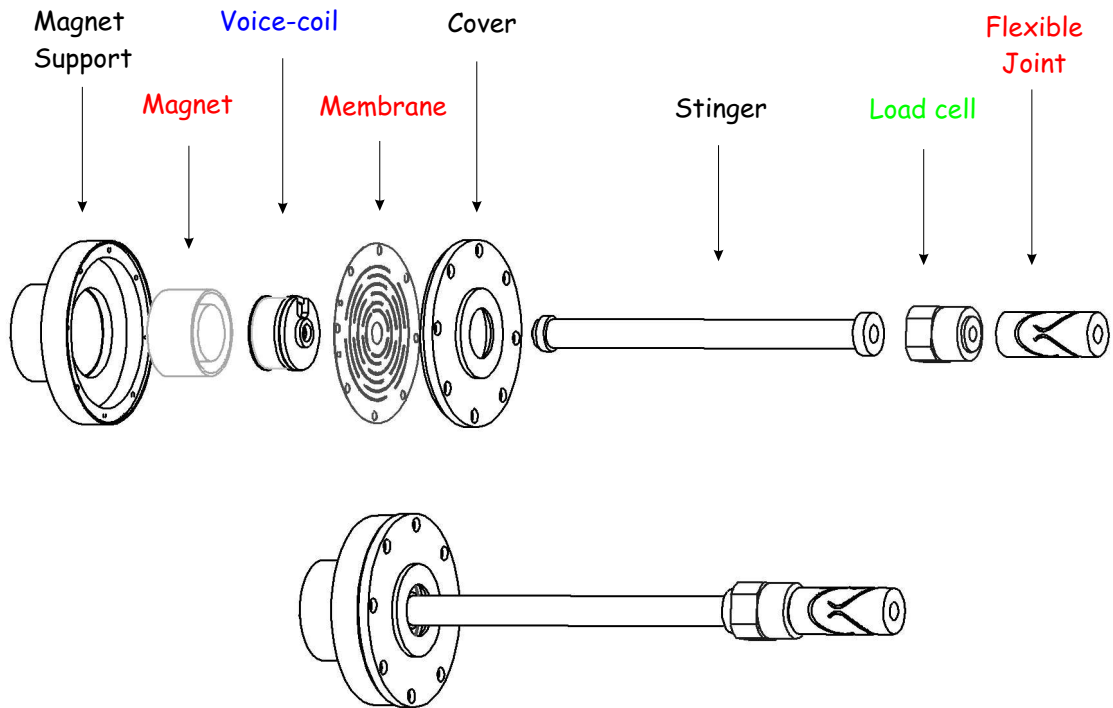


Figure 10. Exploded view of the leg (Design # 2).

## 5.1 Membrane

The membranes are made of Beryllium Copper alloy which is a non magnetic material with high yield stress (a thin film cover was added to avoid corrosion due to metal-metal interaction with the aluminium support). The membrane geometry was optimized to *(i)* maximize the ratio between the radial stiffness and longitudinal stiffness, *(ii)* to achieve a radial stiffness as constant as possible with the longitudinal extension of the leg (the longitudinal extension and the rotation of the stinger axis introduces bending in the membrane), and *(iii)* reduce the stress concentration to improve the fatigue life. Figure 11 shows various membrane geometries which have been tested during the course of this project. The membranes were modelled with finite elements (FE) and a *Guyan reduction* was performed to obtain the various spring constants to be integrated in the global model of the platform. Figure 12 shows typical results of non-linear FE calculations of the evolution of the axial and radial stiffness with the stroke of the leg.

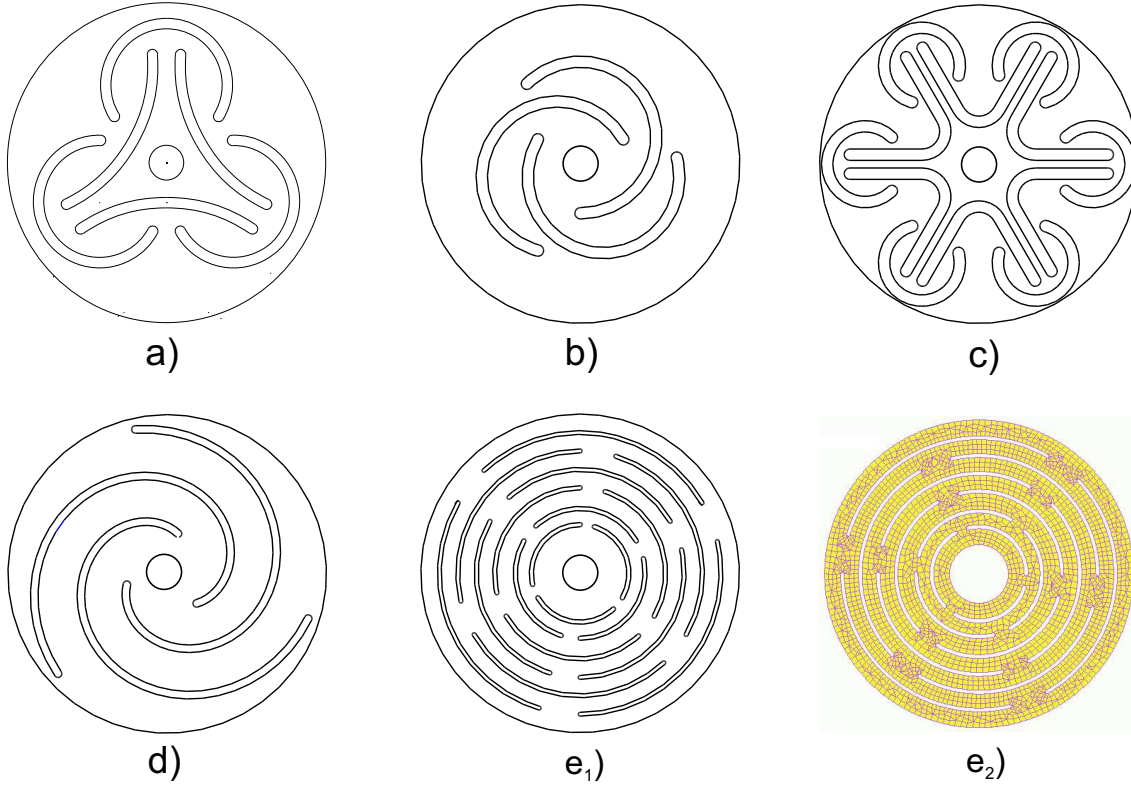


Figure 11. Various membrane geometries and F.E. mesh.

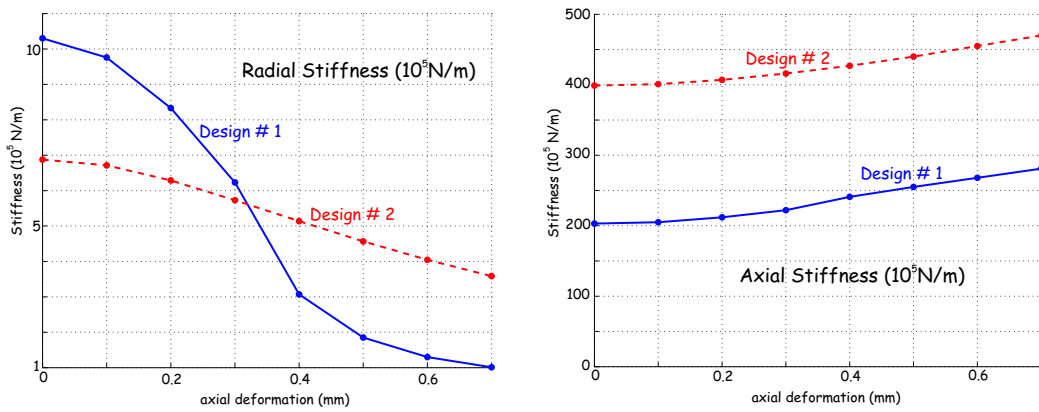


Figure 12. Axial and lateral stiffness as a function of the leg extension.

## 5.2 Voice coil

The magnet assembly used in this project is a radial polarity toroid with ferromagnetic core from BEI Kimco. The gap between the coil and the magnet is large enough to allow the rotation of the stinger by  $1.5^\circ$ . The coil consists of 201 turns on a plastic support (PEEK); this is important to eliminate the eddy currents in a metallic support, which would introduce passive damping in the system, with the detrimental consequences discussed earlier on the asymptotic decay rate. The voice coil maximum force is 2.7 N; the stroke is  $\pm 0.7$  mm.

## 5.3 Stinger

In order to minimize its weight, the stinger consists of a carbon fibre epoxy tube with aluminium connections; in order to limit damage in case of excessive elongation, it is provided with a mechanical stop which limits the stroke at  $+1.5$  mm (in the other direction, the stroke is limited by contact between the coil support and the magnet).

## 5.4 Flexible joint

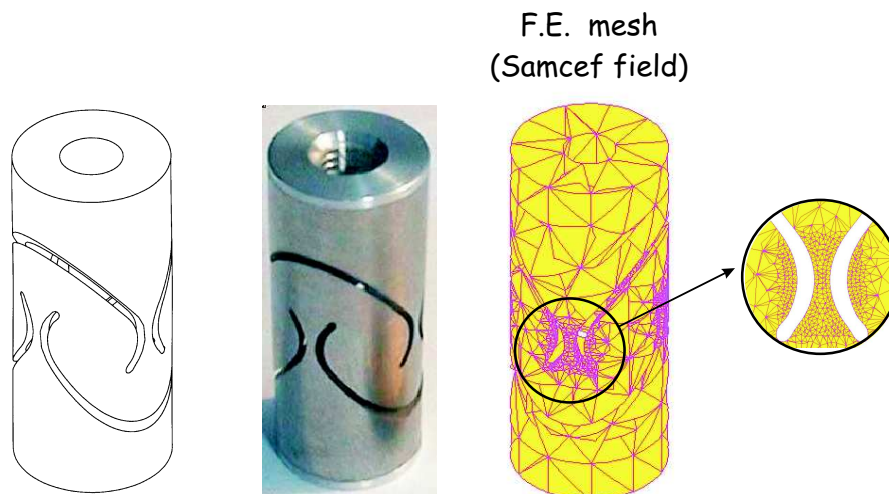


Figure 13. Flexible joint used in this project.

The influence of the flexible joints on the performance of the platform has been stressed earlier in the paper; the joint should behave as close as possible to a spherical joint, that is exhibit high axial and shear stiffness, and low bending and torsional stiffness. On the other hand, the joints play also a key role in the mechanical integrity of the system which would call for strong, and consequently stiff joints. These conflicting requirements have led to extensive numerical studies and prototyping (part of the story is available in [19]). Eventually, we opted for the design of Fig.13, manufactured by electro-erosion. The material selected was NiTiNOL alloy, based on its low Young modulus and high yield strength (respectively  $\sim 60$  GPa and 900-1900

MPa in this case). We also expected to benefit from additional properties of super-elasticity which, we hoped, would add damping to the local transversal modes of the leg, but it did not work out as expected, for unknown reasons (material data were actually extremely difficult to obtain from the manufacturer). In a later version developed at Micromega Dynamics on behalf of ESA/ESTEC, Titanium was used instead of NiTiNOL, because of more reliable material data. The joint profile was studied numerically with FE and a Guyan reduction performed, to obtain the  $12 \times 12$  stiffness matrix of the joint, to be integrated in the global model of the platform.

### 5.5 Model of the isolator

The reduced models of the various components have been assembled in a leg model of small size (less than 100 d.o.f., depending on the configuration), with which a model of the whole platform has been generated. Although small in size, this model is accurate in a wide frequency band, up to about 500 Hz, which is appropriate to evaluate the isolation performance of the system. All F.E. models have been developed in SAMCEF; the dynamic model of the platform has been transformed into state-space and coupled with a control model in MATLAB/SIMULINK. The coupled model has been used extensively to design the components, optimize their shape and size, and tune the controller gain; it was also used to predict the transmissibility matrix. Figure 14 shows a numerical simulation of the experiment which is described below. The vertical transmissibility with control exhibits a small overshoot due to the high-pass filter at 0.5 Hz, the residual stiffness of the spherical joints and the modal spread (for the test configuration,  $\Omega_6/\Omega_1 = 2.2$ ). The performance of the isolator near 100 Hz is -40 dB and the first local modes occur above 400 Hz.

## 6 EXPERIMENT

### 6.1 Experimental set-up

The full platform is shown in Fig.15 (design # 2). In order to measure the six-axis transmissibility, it is equipped with 12 calibrated accelerometers placed at well defined locations on the base and payload plates, so that their motion can be reconstructed. The platform is placed on a shaking table consisting of a rigid slab mounted on springs, and excited by an inertial shaker with adjustable orientation (Fig.16). In addition, two high precision accelerometers are placed on the two plates, to monitor the vertical direction.

### 6.2 Transmissibility

Let  $x_d = (x_{d1}, x_{d2}, x_{d3}, x_{d4}, x_{d5}, x_{d6})^T$  and  $x_c = (x_{c1}, x_{c2}, x_{c3}, x_{c4}, x_{c5}, x_{c6})^T$  be the displacements at the sensor location, respectively on the base plate and the payload plate ( $x_d$  is the input to the isolator system and  $x_c$  the output), and let  $X_d(\omega)$  and  $X_c(\omega)$  be their Fourier transform. The relationship between the readings at the sensors on the payload plate and the base plate can

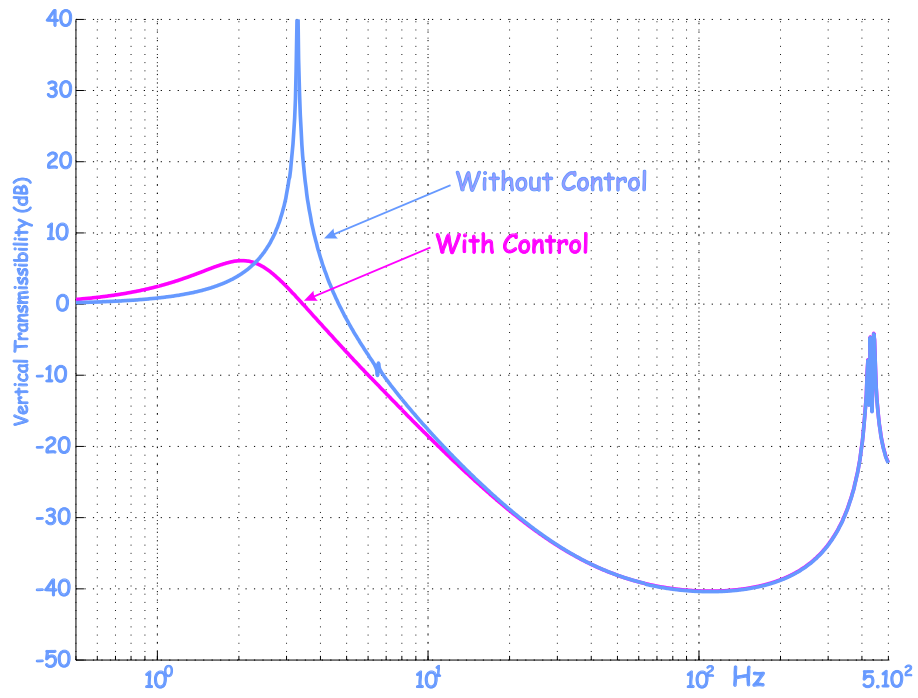


Figure 14. Numerical prediction of the transmissibility in the vertical direction.

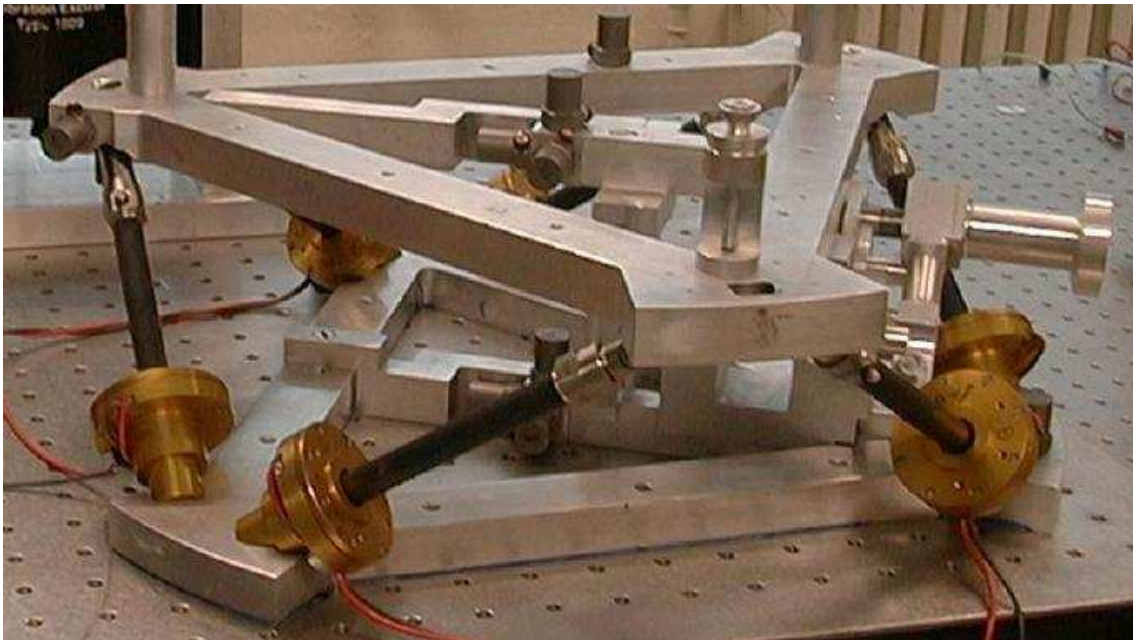


Figure 15. View of the isolator.

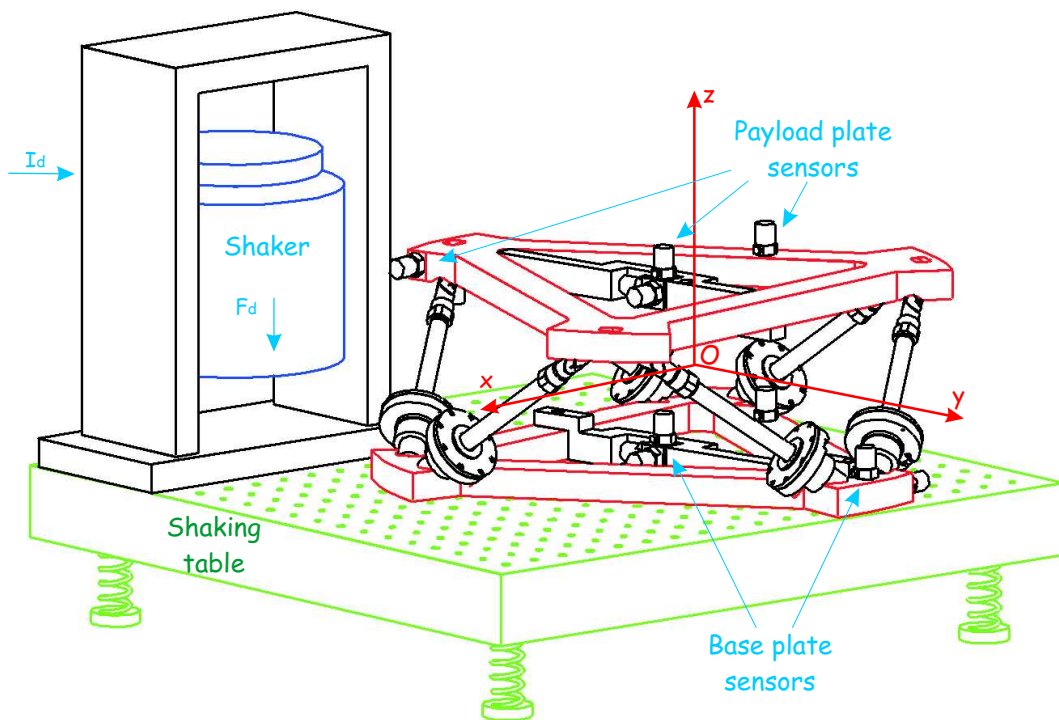


Figure 16. Test set-up for the measurement of the transmissibility matrix.

be expressed using the frequency dependent transmissibility matrix  $T(\omega)$  as follows:

$$X_c(\omega) = T(\omega)X_d(\omega), \quad T(\omega) = \begin{bmatrix} T_{11} & T_{12} & \dots & T_{16} \\ T_{21} & T_{22} & \dots & T_{26} \\ \dots & \dots & \dots & \dots \\ T_{61} & T_{62} & \dots & T_{66} \end{bmatrix} \quad (17)$$

$T_{ij}(\omega)$  represents the displacement at sensor  $i$  of the payload for an imposed displacement of the base  $X_d(\omega) = e_j$ , where  $e_j = (0 \ 0 \dots 1 \dots 0)^T$  is the vector with all entries equal to 0 except entry  $j$  which is equal to 1. The transmissibility matrix is thus dependent on the choice and orientation of the sensors. Next, Assume that the inputs and outputs are transformed into

$$X_d^*(\omega) = T_d X_d(\omega), \quad X_c^*(\omega) = T_c X_c(\omega) \quad (18)$$

where  $T_d$  and  $T_c$  are constant matrices defining geometric transformations. Equation (17) becomes:

$$X_c^*(\omega) = T_c T(\omega) T_d^{-1} X_d^*(\omega) \quad (19)$$

$X_d^*(\omega)$ , and  $X_c^*(\omega)$  are the Fourier transform of the generalized coordinates. The transmissibility matrix between the generalized coordinates reads:

$$T^*(\omega) = T_c T(\omega) T_d^{-1} \quad (20)$$

A natural choice of generalized coordinates which also leads to a clear physical interpretation is the translations  $x, y, z$  and the rotations  $\theta_x, \theta_y, \theta_z$ , of a reference frame located at the geometric center  $O$  of the platform (Fig.16). Thus,  $x_d^* = (x_d, y_d, z_d, \theta_{xd}, \theta_{yd}, \theta_{zd})$  and  $x_c^* = (x_c, y_c, z_c, \theta_{xc}, \theta_{yc}, \theta_{zc})$  are the generalized coordinates of the base plate and the payload plate, respectively, expressed in the same reference frame. In other words,  $x_d^*$  characterizes the motion of the reference frame when it is attached to the base plate, and  $x_c^*$  when it is attached to the payload plate. With this choice, column  $i$  of the transmissibility matrix  $T^*(\omega)$  corresponds to the amplitude of the harmonic response of the payload to an imposed harmonic generalized displacement of the base plate  $X_d^*(\omega) = e_i$ , i.e, a pure translation or a pure rotation of the base plate in a given direction  $x, y$  or  $z$  of the reference frame.

### 6.3 Fröbenius norm

The transmissibility matrix is a  $6 \times 6$  matrix. To interpret the results and assess the performance of the isolator, it is convenient to define a scalar indicator with a meaning similar to that of the transmissibility of a single-axis isolator, which provides for every frequency a measure of the isolation capability of the isolator. The Fröbenius norm is often used for this purpose [7]; it is defined by

$$\|T(\omega)\| = (\text{Trace}[T(\omega)T(\omega)^H])^{1/2} = \left( \sum_{i=1}^6 \sum_{j=1}^6 |T_{ij}(\omega)|^2 \right)^{1/2} \quad (21)$$

where  $^H$  stands for the Hermitian. This norm can be interpreted as follows: From Parseval's theorem,

$$\begin{aligned} \int_{-\infty}^{\infty} x_c^T x_c dt &= \frac{1}{2\pi} \int_{-\infty}^{\infty} X_c(\omega)^H X_c(\omega) d\omega \\ &= \frac{1}{2\pi} \int_{-\infty}^{\infty} \text{Trace}[X_c(\omega) X_c(\omega)^H] d\omega \\ &= \frac{1}{2\pi} \int_{-\infty}^{\infty} \text{Trace}[T(\omega) X_d(\omega) X_d(\omega)^H T(\omega)^H] d\omega \end{aligned} \quad (22)$$

By definition of the energy spectral density, we have:

$$S_{xx} = \frac{1}{2\pi} E[|X(\omega)|^2] \quad (23)$$

Assuming that the motion of the base plate is such that the components of  $X_d(\omega)$  are uncorrelated with unit energy spectral density,

$$\frac{1}{2\pi} E[X_d(\omega) X_d(\omega)^H] = I \quad (24)$$

and Equ.(22) becomes:

$$\begin{aligned} \int_{-\infty}^{\infty} E[x_c^T x_c] dt &= \int_{-\infty}^{\infty} \text{Trace}[T(\omega) \frac{1}{2\pi} E[X_d(\omega) X_d(\omega)^H] T(\omega)^H] d\omega \\ &= \int_{-\infty}^{\infty} \text{Trace}[T(\omega) T(\omega)^H] d\omega = \int_{-\infty}^{\infty} \|T(\omega)\|^2 d\omega \end{aligned} \quad (25)$$

Thus,  $\|T(\omega)\|^2$  represents *the frequency distribution of the energy of the payload plate when the six inputs of the base plate are uncorrelated with unity energy spectral density (uniform over all frequencies)*.

In absence of isolator, the two plates are rigidly linked, and with our choice of coordinates, we have  $x_c^* = x_d^*$ . In this particular case, the transmissibility matrix  $T^*(\omega)$  is the identity matrix and  $\|T^*(\omega)\| = \sqrt{6}$ . Thus, to obtain a performance metric comparable to the transmissibility of a one-axis isolator, one must consider

$$\Gamma(\omega) = \|T^*(\omega)\|/\sqrt{6} \quad (26)$$

The procedure used to identify experimentally the transmissibility matrix is discussed below.

#### 6.4 Identification of the transmissibility

Consider the experimental setup of Fig.16. The base plate is attached to the shaking table to form a rigid body; the payload plate is also a rigid body. In order to identify the transmissibility matrix, it is necessary to input a disturbance force  $f_d$  to the shaking table; this is achieved with an inertial actuator rigidly attached to it; the input force is controlled through the input current  $I_d$  of the shaker. The shaker position and orientation can be adjusted to change the disturbance force  $f_d$ . The current  $I_d$  is recorded during the experiments, but  $f_d$  is not measured. The readings

from the six sensors on each body (accelerometers in this case) are  $X_c(\omega)$  and  $X_d(\omega)$ ; they can be transformed into the generalized coordinates  $X_c^*(\omega)$  and  $X_d^*(\omega)$  using (18).

### General methodology

Since the disturbance force acts on the shaking table which is rigidly linked to the base plate, one can write:

$$\begin{Bmatrix} X_c^*(\omega) \\ X_d^*(\omega) \end{Bmatrix} = \begin{bmatrix} H_{11}(\omega) & H_{12}(\omega) \\ H_{21}(\omega) & H_{22}(\omega) \end{bmatrix} \begin{Bmatrix} 0 \\ F_d(\omega) \end{Bmatrix} \quad (27)$$

From which one gets:

$$X_c^*(\omega) = H_{12}(\omega)H_{22}(\omega)^{-1}X_d^*(\omega) \quad (28)$$

The transmissibility matrix is therefore:

$$T^*(\omega) = H_{12}(\omega)H_{22}(\omega)^{-1} \quad (29)$$

The determination of  $H_{12}(\omega)$  and  $H_{22}(\omega)$  would require six *decoupled* excitations in the direction of the six generalized coordinates of the base plate. Because of the practical limitations with respect to the shaker placement in the experiment, it is generally impossible to fulfill this decoupling requirement. However, it is sufficient to use six *independent* excitations  $F_{di}(\omega)$ ,  $i = 1 \dots 6$ .

In practice, only the current is measured so that we have six different imposed currents  $I_{di}(\omega)$ ,  $i = 1 \dots 6$  corresponding to 6 *independent* shaker orientations. The FRF between the responses of the payload and the base, and the six imposed currents are computed and arranged as the columns of a matrix:

$$\begin{aligned} H_d(\omega) &= [H_{d1}, H_{d2}, H_{d3}, H_{d4}, H_{d5}, H_{d6}] \\ H_c(\omega) &= [H_{c1}, H_{c2}, H_{c3}, H_{c4}, H_{c5}, H_{c6}] \end{aligned} \quad (30)$$

where

$$H_{di}(\omega) = \frac{X_{di}(\omega)}{I_{di}(\omega)} \quad (31)$$

is the column vector of the 6 FRF between the 6 sensor displacements of the base plate and the  $i^{th}$  imposed current ( $H_{ci}(\omega)$  is defined in the same way for the payload).

It follows from (17) that:

$$H_c(\omega) = T(\omega)H_d(\omega) \quad (32)$$

If the shaker orientations have been selected in such a way that  $H_d(\omega)$  is invertible, one finds:

$$T(\omega) = H_c(\omega)H_d(\omega)^{-1} \quad (33)$$

### Redundant measurements

If more than 6 excitations are used, the matrices  $H_d(\omega)$  and  $H_c(\omega)$  have more than 6 columns. The transmissibility matrix can still be computed from (33) using the Moore-Penrose pseudo-inverse:

$$T(\omega) = H_c(\omega)H_d(\omega)^+ \quad (34)$$

where the pseudo-inverse of the matrix is defined by

$$H_d^+ = H_d^H (H_d H_d^H)^{-1} \quad (35)$$

(in practice, a singular value decomposition is used, and singular values smaller than a tolerance are treated as zero and deleted in the calculation of the pseudo-inverse). Once  $T(\omega)$  has been estimated, the transmissibility in generalized coordinates,  $T^*(\omega)$ , can be computed by (20).

### Simplifications in the procedure

The procedure described assumes that the transmissibility matrix is fully populated. In practice however, computations have shown that some terms are dominant when the transmissibility is expressed in generalized coordinates and the following form of the transmissibility matrix can be assumed:

$$T^*(\omega) = \begin{bmatrix} T_{11} & T_{12} & 0 & T_{14} & T_{15} & 0 \\ T_{21} & T_{22} & 0 & T_{24} & T_{25} & 0 \\ 0 & 0 & T_{33} & 0 & 0 & 0 \\ T_{41} & T_{42} & 0 & T_{44} & T_{45} & 0 \\ T_{51} & T_{52} & 0 & T_{54} & T_{55} & 0 \\ 0 & 0 & 0 & 0 & 0 & T_{66} \end{bmatrix} \quad (36)$$

With this assumption, one can see that  $T_{33}$  and  $T_{66}$  are computed as follows:

$$T_{33}(\omega) = \frac{Z_c(\omega)}{Z_d(\omega)}, \quad T_{66}(\omega) = \frac{\theta_{zc}(\omega)}{\theta_{zd}(\omega)} \quad (37)$$

and a single excitation is sufficient to determine both terms, provided the motions  $Z_d(\omega)$  and  $\theta_{zd}(\omega)$  are sufficiently excited. The other terms of the transmissibility matrix can be computed using the procedure described above, considering the reduced transmissibility matrix:

$$T^*(\omega) = \begin{bmatrix} T_{11} & T_{12} & T_{14} & T_{15} \\ T_{21} & T_{22} & T_{24} & T_{25} \\ T_{41} & T_{42} & T_{44} & T_{45} \\ T_{51} & T_{52} & T_{54} & T_{55} \end{bmatrix} \quad (38)$$

there are only four generalized degrees of freedom for the payload and the base. In this case, four independent excitations are needed. This approach has been used to assess the performance of the Stewart platform during the parabolic flight.

### Results

Experiments have been conducted in the laboratory and in zero-gravity during the 38<sup>th</sup> ESA parabolic flight campaign. For the ground tests, the gravity was compensated by hanging the payload from three soft elastic springs holding the corners of the upper triangle; a mechanism allowed to adjust the spring tension in such a way that the length of the legs are close to their nominal value. The holding mechanism introduces an additional stiffness which increases the corner frequency of the isolator. During the parabolic flight tests, the zero-gravity environment

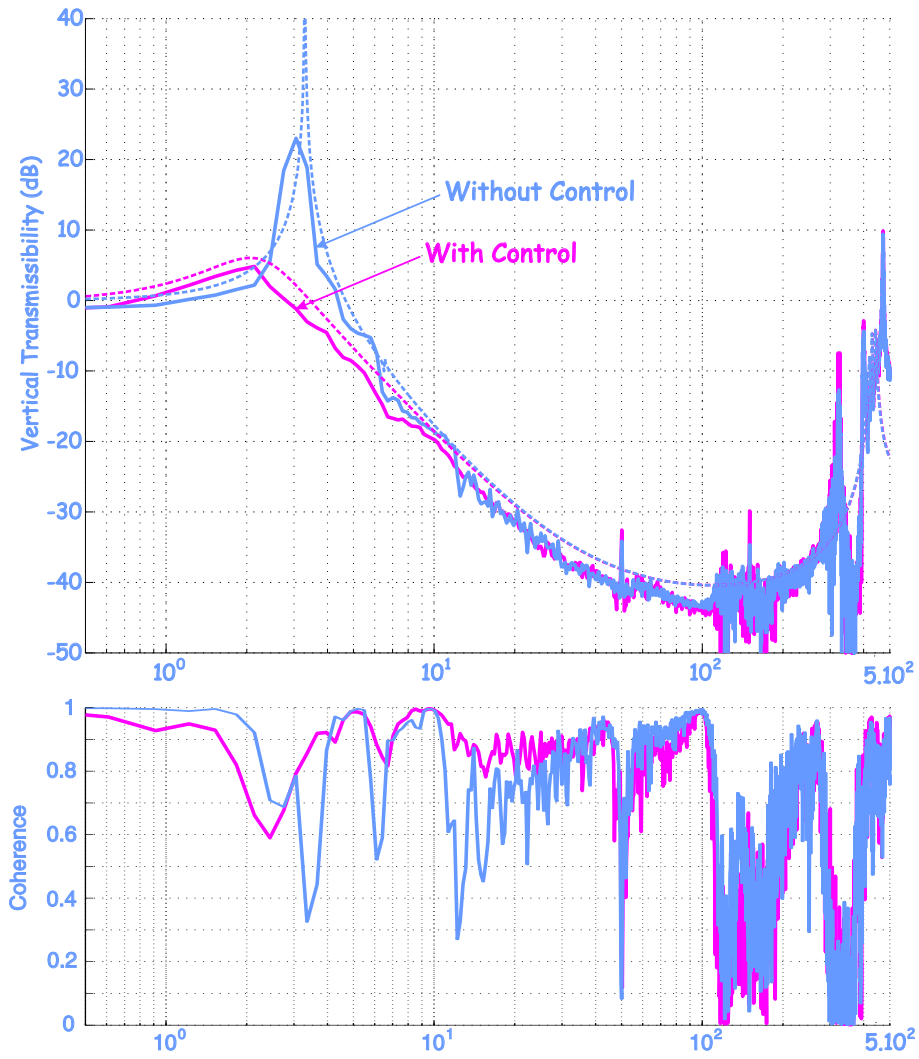


Figure 17. (a) Experimental transmissibility in the vertical direction, with and without control. (b) Coherence function, with and without control.

can be maintained only during 20 sec, which reduces the useful part of the signal to about 15 sec. This leads to practical difficulties to achieve meaningful results at very low frequency and to eliminate the noise in frequency bands where the transmissibility is low. Fortunately, the flight campaign included 90 parabolas which allowed some averaging to be performed.

Figure 17(a) shows the experimental vertical transmissibility obtained from data measured with the high precision accelerometers during the parabolic flight tests, with and without control; the numerical simulations of Fig.14 are also shown in dotted lines in this figure, for comparison purposes; the agreement between the experiment and the simulation is very good. Figure 17(b) shows the coherence function measured during the same tests and gives an idea of the quality of the collected data. Single-axis transmissibilities measured along the horizontal axes are very similar to that in the vertical direction. Figure 18 shows the Fröbenius norm  $\Gamma(\omega)$  as defined by (26) and calculated from the measurements of the 12 regular accelerometers; the simulation results are again shown in dotted line in the figure; the agreement between the experiments and the simulations is also good, although not as good as in Fig.17 (which has been obtained with high precision accelerometers). A detailed examination of the results shows that the main source of discrepancy between the values of  $\Gamma(\omega)$  computed from the simulation results and the measured data originates from the non-diagonal terms of the transmissibility matrix which are more sensitive to noise.

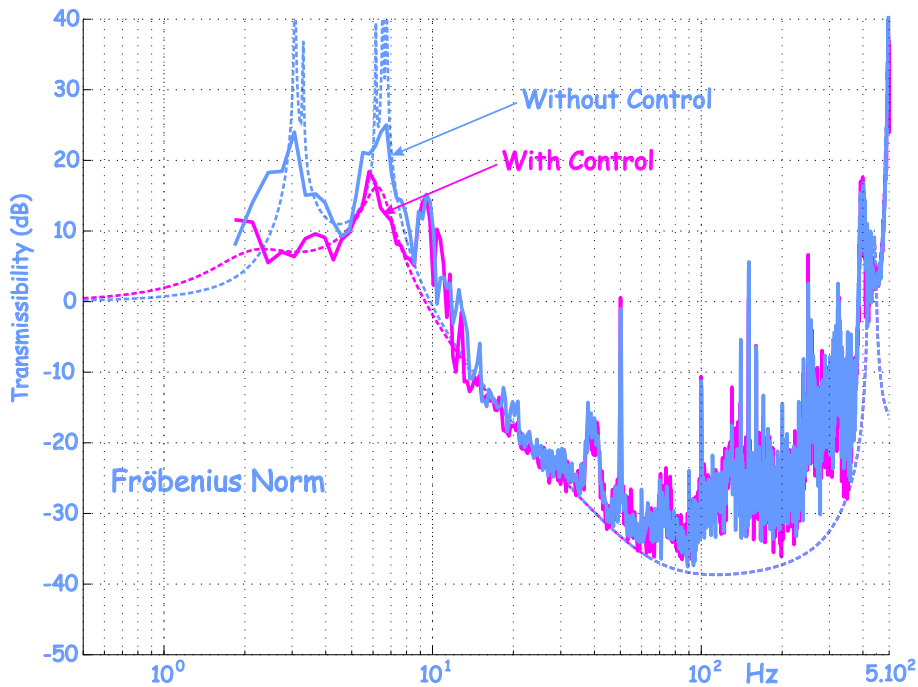


Figure 18. Fröbenius norm  $\Gamma(\omega)$  as defined by (26), with and without control. The full lines refer to experiments and the dotted line to simulation results.

## 7 CONCLUSION

This paper summarizes the effort that has been conducted at ULB over the past 5 years on the development of an active vibration isolator for precision payloads. The first part of this paper recalls the principles of active isolation and summarizes the main theoretical results for multiple axis decentralized control based on force feedback. The second part discusses the technology and describes the evolution of the design over the five years of the project. The third part is devoted to the experimental set-up and the performance evaluation; a technique for the evaluation of the  $6 \times 6$  transmissibility matrix is described. Zero-gravity tests in parabolic flight are also reported; they show that the isolator is efficient in a frequency band between 5 Hz and 400 Hz, with a maximum attenuation of -40 dB in the vicinity of 100 Hz. There is a close agreement between the experimental results and the transmissibility predicted by numerical simulations. It is interesting to note that the performance improvement with respect to the previous parabolic flight performed two years earlier (frequency band: 5 Hz - 100 Hz, maximum attenuation of -20 dB [19]) has been obtained only by mechanical redesign of the leg.

## 8 ACKNOWLEDGMENT

This study was supported by the Inter University Attraction Pole IUAP 5 on *Advanced Mechatronics Systems*, and by ESA/ESTEC in the framework of the programs: *PRODEX: 38<sup>th</sup> ESA parabolic flight campaign, Bordeaux 26-28 October 2004*, and *GSTP:LSSP, Low Stiffness Stewart Platform*.

## REFERENCES

- [1] Laskin, R.A., Sirlin, S.W., Future payload isolation and pointing system technology, *AIAA J. of Guidance and Control*, 9, 469-477, 1986.
- [2] Collins, S.A., von Flotow, A.H., Active vibration isolation for spacecraft, 42<sup>nd</sup> IAF Congress, paper No IAF-91-289, Montreal, Oct.1991.
- [3] Rivin, E.I., *Passive Vibration Isolation*, ASME Press, N-Y, 2003.
- [4] Karnopp, D.C., Trikha, A.K., Comparative study of optimization techniques for shock and vibration isolation, *Trans. ASME, J. of Engineering for Industry, Series B*, 91, 1128-1132, 1969.
- [5] Kaplow, C.E., Velman, J.R., Active local vibration isolation applied to a flexible telescope, *AIAA J. of Guidance and Control*, 3, 227-233, 1980.
- [6] Geng, Z. Haynes, L., Six degree of freedom active vibration isolation system using the Stewart platforms, *IEEE Transactions on Control Systems Technology*, Vol.2, No 1, 45-53, 1994.
- [7] Spanos, J., Rahman, Z., Blackwood, G., A soft 6-axis active vibration isolator, Proc. of the *IEEE American Control Conference*, 412-416, 1995.
- [8] Rahman, Z.H, Spanos, J.T, Laskin, R.A., Multi-axis vibration isolation, suppression and steering system for space observational applications, *SPIE Symposium on Astronomical*

- Telescopes and Instrumentation, Kona-Hawaii, March 1998.
- [9] Thayer, D., Vagners, J., von Flotow, A., Hardman, C., Scribner, K., Six-axis vibration isolation system using soft actuators and multiple sensors; *AAS 98-064*, 497-506, 1998.
  - [10] [Thayer, D., Campbell, M., Vagners J., von Flotow, A., Six-Axis vibration isolation system using soft actuators and multiple sensors, \*J. of Spacecraft and Rockets\*, Vol.39, No 2, 206-212, March-April 2002.](#)
  - [11] [Hauge, G.S., Campbell, M.E., Sensors and control of a spaced-based six-axis vibration isolation system, \*J. of Sound and Vibration\*, 269, 913-931, 2004.](#)
  - [12] [McInroy, J.E., O'Brien, J.F., Neat, G.W., Precise, fault-tolerant pointing using a Stewart platform, \*IEEE/ASME Transactions on Mechatronics\*, Vol.4, No 1, 91-95, March 1999.](#)
  - [13] [McInroy, J.E., Neat, G.W., O'Brien, J.F., A robotic approach to fault-tolerant, precision pointing, \*IEEE Robotics and Automation Magazine\*, 24-37, Dec. 1999.](#)
  - [14] [McInroy, J.E., Hamann, J., Design and control of flexure jointed hexapods, \*IEEE Transaction on Robotics\*, 16\(4\), 372-381, August 2000.](#)
  - [15] [McInroy, J.E., Modeling and design of flexure jointed Stewart platforms for control purposes, \*IEEE/ASME Transaction on Mechatronics\*, 7\(1\), March 2002.](#)
  - [16] [Stewart, D., A platform with six degrees of freedom, \*Pro. Instn. Mech. Engrs.\*, 180\(15\), 371-386, 1965-66.](#)
  - [17] [Preumont, A., François, A., Bossens, F., Abu-Hanieh, A., Force feedback versus acceleration feedback in active vibration isolation, \*J. of Sound and Vibration\*, 257\(4\), 605-613, 2002.](#)
  - [18] [Preumont, A., \*Vibration Control of Active Structures, An Introduction\*, 2nd Edition, Kluwer, 2002.](#)
  - [19] [Abu Hanieh, A., \*Active Isolation and Damping of Vibrations via Stewart Platform\*, PhD Thesis, ULB-Active Structures Laboratory, Brussels, Belgium, 2003.](#)